Covalently Bonded Graphene–Carbon Nanotube Hybrid for High-Performance Thermal Interfaces

Jie Chen, Jens H. Walther,* and Petros Koumoutsakos**

The remarkable thermal properties of graphene and carbon nanotubes (CNTs) have been the subject of intensive investigations for the thermal management of integrated circuits. However, the small contact area of CNTs and the large anisotropic heat conduction of graphene have hindered their applications as effective thermal interface materials (TIMs). Here, a covalently bonded graphene–CNT (G-CNT) hybrid is presented that multiplies the axial heat transfer capability of individual CNTs through their parallel arrangement, while at the same time it provides a large contact area for efficient heat extraction. Through computer simulations, it is demonstrated that the G-CNT outperforms few-layer graphene by more than 2 orders of magnitude for the *c*-axis heat transfer, while its thermal resistance is 3 orders of magnitude lower than the state-of-the-art TIMs. We show that heat can be removed from the G-CNT by immersing it in a liquid. The heat transfer characteristics of G-CNT suggest that it has the potential to revolutionize the design of high-performance TIMs.

1. Introduction

In the last 30 years, along with advances in the miniaturization of the electronic devices, we have witnessed a staggering escalation of the power density in integrated circuit (IC) chips. Today, the power density on a modern microprocessor reaches 100 W cm^{-2}, an order of magnitude higher than that of a typical hot plate.[1] Thermal management has become a critical aspect in the design of ICs, as heat dissipation drastically limits the performance and reliability of the devices, and large amounts of energy are required for their cooling.[1] Furthermore, as the next generation of ICs are expected to rely on chip stacking, novel 3D solutions must be devised for their heat management.[2]

The heat dissipation in ICs is mediated by the thermal interface materials (TIMs) that fill the gap between the conducting surfaces to reduce the interfacial thermal (Kapitza) resistance. State-of-the-art TIMs, such as thermal greases and gels, have a typical thermal resistance of around 10 mm^2 K W^{-1}.[3] Graphene and carbon nanotubes (CNTs) hold a great potential for the development of advanced TIMs due to their extraordinarily high thermal conductivity (around 3000–5000 W m^{-1} K^{-1}[4]). The thermal properties of graphene and CNTs have been the subject of intensive recent investigations.[5–14] However, a number of issues need to be resolved before they can be used in engineering applications. When CNTs are in contact with another surface, their small diameter results in a large contact thermal resistance that dominates the overall thermal resistance.[15] As a result, CNTs need to be dispersed in a matrix, such as a polymer, to ensure a large contact area. However, the high Kapitza resistance between the CNTs and the matrix[16] drastically reduces the thermal conductivity of such CNT composites. The resulting thermal conductivity of the composite is close to that of a polymer matrix (around 0.3 W m^{-1} K^{-1} at room temperature).[17] Moreover, Gulotty et al.[18] found that thermal conductivity of the CNT–polymer composites can be improved via the carboxylic functionalization of multiwall CNTs. In contrast to CNTs, graphene provides a large contact area to mediate the heat transfer. Nevertheless, while graphene has a superior in-plane thermal conductivity (around 5000 W m^{-1} K^{-1} at room temperature[19]), its cross-plane heat transfer is hindered by the large interlayer thermal resistance: the *c*-axis thermal conductivity in few-layer graphene (FLG) is only around 0.7 W m^{-1} K^{-1}.[20]

Hence, reducing the *c*-axis thermal resistance in FLG[13] is a key issue in developing graphene-based TIMs. In this context, the covalently bonded carbon hybrids have attracted much interest recently.[21–26] In particular, the 3D stacking of the “pillared graphene” structure[21] has shown promising applications in the hydrogen storage[21] and heat transfer.[24] Here, we propose an sp^2 covalently bonded graphene–CNT hybrid structure (which we have termed as G-CNT) that reduces drastically the *c*-axis thermal resistance of FLG. We demonstrate through molecular dynamics (MD) simulations that thermal transport between FLG sheets is clearly enhanced when the covalent

Dr. J. Chen, Prof. P. Koumoutsakos
Computational Science and Engineering Laboratory
ETH Zurich
CH-8092 Zurich, Switzerland
E-mail: jiechen@ethz.ch; petros@ethz.ch
Dr. J. Chen
Center for Phononics and Thermal Energy Science
School of Physics Science and Engineering
Institute for Advanced Study
Tongji University
Shanghai 200092, P. R. China
E-mail: jie@tongji.edu.cn
Prof. J. H. Walther
Department of Mechanical Engineering
Technical University of Denmark
DK-2800 Kgs. Lyngby, Denmark
E-mail: jhw@mek.dtu.dk

DOI: 10.1002/adfm.201501593

© 2015 WILEY-VCH Verlag GmbH & Co. KGaA, Weinheim

bonding replaces the noncovalent van der Waals (vdW) interactions. We find that the G-CNT hybrid structure possesses advantageous heat transfer properties over individual CNT, while at the same time it provides a large contact area to facilitate the heat transfer from planar surfaces. With 10% CNT bonding, the cross-plane thermal transport in the G-CNT can be enhanced by more than 2 orders of magnitude over that of FLG. The estimated thermal resistance of the hybrid G-CNT structure at the typically bond line thickness[3] of 10 µm is 3 orders of magnitude lower than that of state-of-the-art TIMs. We have conducted phonon wave packet simulations to elucidate the difference in the energy transmission between the sp^2 covalent bonding and noncovalent vdW interaction.

2. Results and Discussion

2.1. Thermal Conductivity of G-CNT

We first consider two graphene sheets with a cross section $D \times D$ (here $D \approx 10$ nm) covalently bonded to (6,6) CNTs with a fixed length $L = 16$ nm (the simulation domain size for obtaining the asymptotical *c*-axis thermal resistance in FLG[13]). Details about the construction of the G-CNT structure are presented in the Supporting Information. We use two definitions of the cross section when computing the heat flux in the G-CNT: (a) the constant cross section $S_0 = D^2$; (b) the effective cross section excluding the hollow area $S_E = S_0 \times (1 - \rho)$. Here ρ is the density of CNT defined as $\rho = N \times \pi \times R^2/S_0$, where N is the number of CNTs and R is the CNT radius. The thermal conductivity of the G-CNT (setup shown in **Figure 1**a) is computed with the non-equilibrium molecular dynamics (NEMD) simulation. Its *c*-axis thermal conductivity (κ) is almost one order of magnitude higher than that of FLG even with only one CNT. More importantly, κ increases monotonically with ρ (Figure 1b).

We consider two different CNT density regions when constructing the G-CNT structure. In the low CNT density region ($\rho < 20\%$), we set the minimum inter-CNT distance ($d_{\min}$) much larger than the LJ interaction parameter σ ($d_{\min} > 3\sigma$) so that LJ interaction between the CNTs is negligible. As a result, κ of the G-CNT is independent of the specific CNT arrangement for the same CNT density (Figure S5, Supporting Information). Furthermore, we note that using the two definitions of cross section gives equivalent results. This suggests that the improvement of the *c*-axis thermal conductivity in the G-CNT over FLG is due to the replacement

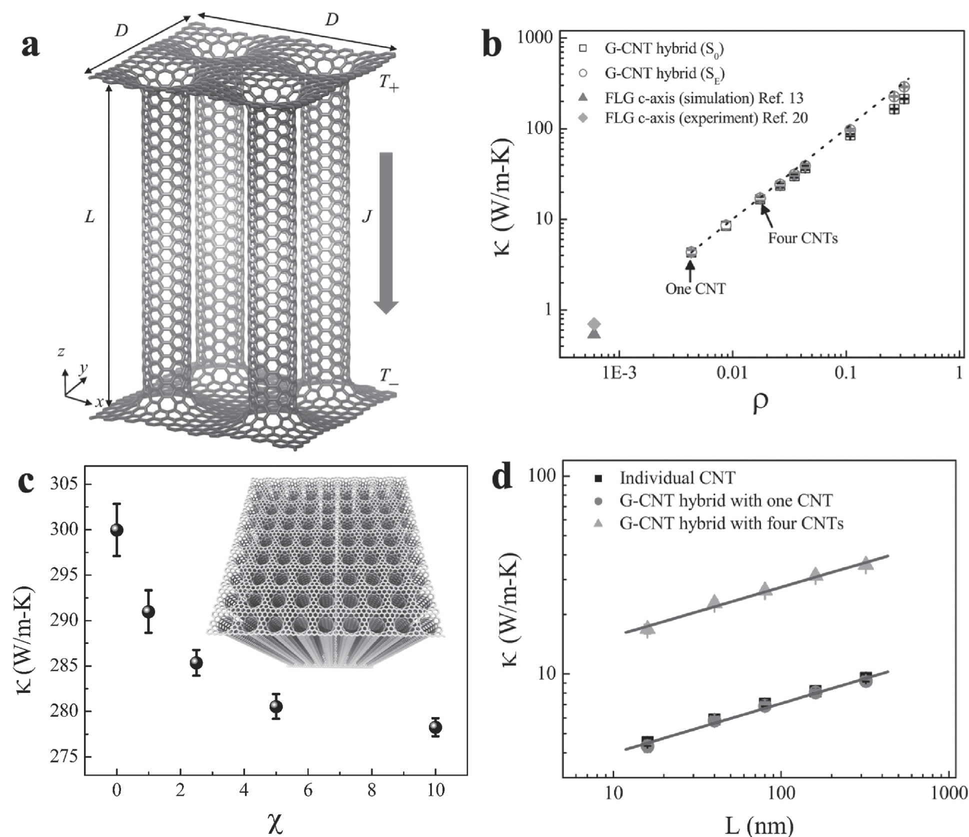

Figure 1. Cross-plane thermal conductivity κ of G-CNT hybrid structure at room temperature. a) Schematic of the setup for the NEMD simulations. Langevin thermostat with temperature T_+ and T_- is applied to the top (red) and bottom (blue) graphene sheets, respectively, resulting in the heat flow in the *z*-direction. b) Dependence of κ on CNT density ρ with the fixed $D = 10$ nm and $L = 16$ nm. Two definitions of cross section (S_0 and S_E) are used for comparison. The *c*-axis thermal conductivity in few-layer graphene from refs. [13,20] is also plotted for reference. The dashed line draws the linear dependence on ρ for reference. c) Effect of inter-CNT interaction strength χ for a CNT array (inset) with $\rho \approx 32\%$, $D = 10$ nm, and $L = 16$ nm. S_E is used in the calculation. *d*, length dependence of κ for individual CNT and G-CNT hybrid structure with $D = 10$ nm. S_0 is used for both G-CNT hybrid structure and individual CNT.

© 2015 WILEY-VCH Verlag GmbH & Co. KGaA, Weinheim
Adv. Funct. Mater. 2015, DOI: 10.1002/adfm.201501593

of noncovalent interaction with covalent bonding. When ρ is below 5%, κ varies linearly with the CNT density (Figure 1b). At 10% CNT density, the κ of the G-CNT is about 100 W m^{-1} K^{-1} (Figure 1b), more than 2 orders of magnitude higher than that of FLG.

In the high CNT density region (ρ > 20%), the inter-CNT distance is within the cutoff distance so that the LJ interaction is no longer negligible, and we construct periodic array of CNTs (phononic crystal structure) with the equal spacing (inset in Figure 1c). For the high-density case, κ is underestimated with S_0 as there are significantly less atoms conducting heat from the holey graphene sheet compared to the full graphene sheet. Moreover, κ exhibits a sublinear dependence at high CNT density (Figure 1b), suggesting an enhanced phonon scatterings. In addition, we find that the inter-CNT interaction also plays a role in the *c*-axis heat transfer. Increasing the inter-CNT interaction strength is found to decrease the κ of the G-CNT monotonically (Figure 1c). This result is consistent with the finding[27,28] that the inter-CNT interaction in multiwalled CNTs is responsible for the reduction of axial thermal conductivity.

2.2. Comparison with Other Structures

We compare the thermal properties of the G-CNT with an individual CNT. The room temperature thermal conductivity of a (6,6) CNT (computed with a similar setup in Figure S4, see the Supporting Information) exhibits a power-law dependence on its length as $\kappa \sim L^{\alpha}$ ($0 < \alpha < 1$), consistent with previous studies.[29,30] This length dependence is due to the break down of Fourier's law in nanostructures.[31,32] The exponent α depends on the temperature and chirality of the CNT,[29,30] and for the (6,6) CNT it is found to be approximately equal to 0.25. To make a direct comparison with the G-CNT, we use the same the cross section S_0 when computing the thermal conductivity of the CNT. In this way we find that the thermal conductivity of the individual CNT is almost identical to that of the G-CNT with only one CNT (Figure 1d). This suggests that the high thermal conductivity of CNTs can be preserved by the G-CNT hybrid. As the single-walled CNTs have higher thermal conductivity than the multiwalled CNTs due to the inter-CNT interaction,[27,28] we expect that multiwalled G-CNT hybrid should have a lower thermal conductivity than the single-walled counterpart. To focus on the idea of covalent bonding, we limit our discussion on the single-walled G-CNT hybrid in this study. Furthermore, with multiple CNTs, the total thermal conductivity of the G-CNT is a multiple of that of the individual CNT (Figure 1d). Due to the sublinear dependence of the CNT thermal conductivity on its length, the parallel arrangement of CNTs in the G-CNT provides a far superior thermal conductivity than that of a single CNT with an equivalent total length. The G-CNT presents a novel avenue to exploit the high thermal conductivity of CNTs.

We note that the typical bond line thickess of the CNT-based state-of-the-art TIMs is L = 10 μm.[33] MD simulations for CNTs at such length scales are beyond our computational resources. Instead we estimate the thermal resistance based on our present results by postulating that the power-law dependence $\kappa \sim L^{\alpha}$ ($\alpha \approx 0.25$) holds in the sub-10 μm length scale. This assumption is consistent with a previous experimental study that reports breakdown of Fourier's law in CNTs with length up to 10 μm.[31] Hence, the thermal resistance depends on the length according to the following relation: $R = L/\kappa \sim L^{1-\alpha}$. As shown in Figure 1b, thermal conductivity $\kappa \approx$ 100 W m^{-1} K^{-1} for the hybrid structure with CNT density ρ = 10% at L = 16 nm, and the corresponding thermal resistance is $R_0 = 1.6 \times 10^{-4}$ mm^2 K W^{-1}. For the same CNT density, the thermal resistance at L = 10 μm can be estimated as $R = R_0 \times (10\,000/16)^{0.75} = 0.02$ mm^2 K W^{-1}. We remark that this value is 3 orders of magnitude lower than the one exhibited by the state-of-the-art TIMs (around 10 mm^2 K W^{-1}).[3,33]

Compared to the pillared graphene,[21] the G-CNT allows for much higher CNT density and as such it enables higher *c*-axis thermal conductivity. It is important to note also that the pillared graphene architecture entails numerous CNT-graphene junctions due to the 3D stacking. These junctions are responsible for the thermal resistance for both in-plane[24] and *c*-axis[26] heat transfer in the pillared graphene. In contrast, CNTs are only covalently bonded with the top and bottom graphene layers in the G-CNT structure. Thus, the G-CNT architecture is more advantageous as it is easier to be realized experimentally[22] and exhibits reduced *c*-axis thermal resistance. Given the available techniques[34–36] for synthesizing the hybrid structure of graphene and CNT, we expect the G-CNT structure proposed in this study can be readily fabricated in experiment.

There are experimental efforts of designing graphene/CNT based composites for novel thermal management.[37–40] For instance, Shahil and Balandin[37] synthesized graphene–FLG nanocomposite polymer and achieved around 23 times enhancement in thermal conductivity at the filler loading faction of 10 vol%, with thermal conductivity reaching around 5.1 W m^{-1} K^{-1} at room temperature. Koo et al.[40] reported the thermal properties of a set of different Li-ion battery electrodes enhanced with multiwalled CNTs. They achieved the highest in-plane and cross-plane thermal conductivity around 141 and 3.6 W m^{-1} K^{-1}, respectively. Depending on the system parameters, the cross-plane thermal conductivity of G-CNT presented in this study (Figure 1) can be an order of magnitude higher than the experimental results. This is because we only consider defect-free G-CNT in our simulation, and the covalent bonding greatly reduces the thermal boundary resistance (see the following discussion) compared to that of the graphene/CNT based nanocomposite used in experiments.

2.3. Phonon Wave-Packet Analysis

In order to understand the enhancement of the *c*-axis thermal conductivity by the covalent bonding, we investigate the propagation of the individual phonon wave packet in graphene sheets with and without covalent bonding to a CNT of length L = 10 nm (**Figure 2**). As the thermal transport is dominated by the acoustic phonons, we focus on the acoustic phonon wave-packet propagation in the [100] direction.

© 2015 WILEY-VCH Verlag GmbH & Co. KGaA, Weinheim

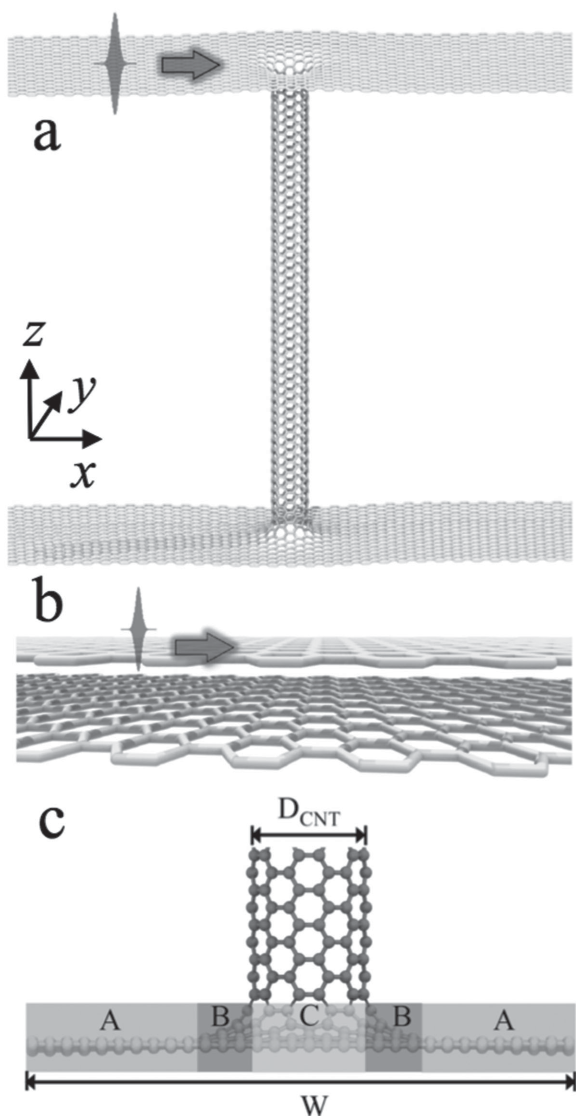

Figure 2. Setup for the phonon wave-packet simulation. A Gaussian wave packet is applied only to the top graphene layer, propagating along the *x*-direction. The simulation domain has about 1000 unit cells in the *x*-direction. a) G-CNT with a single CNT of length $L = 10$ nm. b) Bilayer graphene. c) Region definitions in the top graphene layer along the width direction. Region C has the width of one CNT diameter. Region B is close to CNT, exhibiting surface curvature. Region A is far away from CNT without surface curvature.

In the presence of the covalent bonding, the longitudinal acoustic (LA) wave packet propagates through the CNT to the bottom layer. When the phonon wavelength is greater than the CNT diameter, the wave packet propagation is barely affected by the CNT (**Figure 3**a). With the decrease of the phonon wavelength, the wave packet experiences more scattering by the CNT (Figure 3b), leading to the decreasing phonon transmission coefficient η (Figure 3c). For the transverse acoustic (TA) and flexural acoustic (ZA) phonons, η shows a nonmonotonic dependence on wavenumber due to the complex mode conversion in the G-CNT (see the Supporting Information for details). A similar drop in the transmission coefficient for the low-frequency TA phonons has been observed at CNT/graphene/Si interface.[41]

Without covalent bonding, the wave packet energy is transmitted to the bottom layer through the out-of-plane vibration. Due to the mode orthogonality, we observe negligible out-of-plane vibration when the in-plane phonon wave packet is applied. Therefore, the amplitude of the in-plane wave packet in the top layer is almost unaffected by the inter-layer vdW interaction, causing negligible energy transmission to the bottom layer (Figure 3d). When the ZA wave packet is applied to the top layer, it induces large energy oscillation in both layers at the beginning (the transient state), while the induced energy is distributed equally between two layers in the steady state (Figure 3e). Our wave packet simulations are in line with the recent findings[42–44] showing that the vdW interaction between graphene and substrate has a stronger impact on the out-of-plane phonons than the in-plane phonons.

Figure 3f reports the transmission coefficient η in bilayer graphene for the same wave-packet propagation time as in the G-CNT. In bilayer graphene, negligible in-plane phonon energy (less than 0.5%) can be transmitted to the bottom layer through the noncovalent interaction. For the ZA branch, at most 50% of the energy can be transmitted across the bilayer graphene and only for the low-frequency phonons. If we only consider the nearest-layer interaction in FLG, then the energy transmission across FLG approximately scales as η^{N-1}, where N is the number of layers and η is the transmission coefficient in bilayer graphene. For the same thickness of 10 nm (30 layers in FLG), the estimated energy transmission to the bottom layer in FLG for all acoustic phonon branches will become negligible compared to that in the G-CNT (Figure 3c). The wave-packet simulations clearly elucidate that the phonon transmission across graphene sheets can be significantly promoted by the covalent bonding, leading to the remarkably improved *c*-axis thermal transport in the hybrid structure.

2.4. Cooling of Hot Surfaces

The proposed G-CNT structure is compatible with the multiple stackings envisioned for the next generation 3D IC chips. The G-CNT can serve as a TIM to dissipate the heat from two hot surfaces through the contact with its graphene layers, and it can be immersed in a circulating liquid (**Figure 4**a) for the sustained cooling of IC chips. To demonstrate this idea, we simulate the transient cooling process of the hot surface by G-CNT. The G-CNT and the FLG have the same dimension of $12 \times 10 \times 13$ nm^3, and the G-CNT has a CNT density about 14%. To fill in the empty space between the CNTs in the G-CNT, the number of water molecules (46 111) is chosen to reproduce the bulk water density in the regions away from the CNT and graphene surface.

We first examine the cooling performance of the G-CNT in vacuum, by comparing its transient heat dissipation and temperature relaxation time with that of the FLG having the same dimension. We find that the G-CNT (CNT density around 14%) can cool down the hot surfaces much faster than the FLG

© 2015 WILEY-VCH Verlag GmbH & Co. KGaA, Weinheim
Adv. Funct. Mater. 2015,
DOI: 10.1002/adfm.201501593

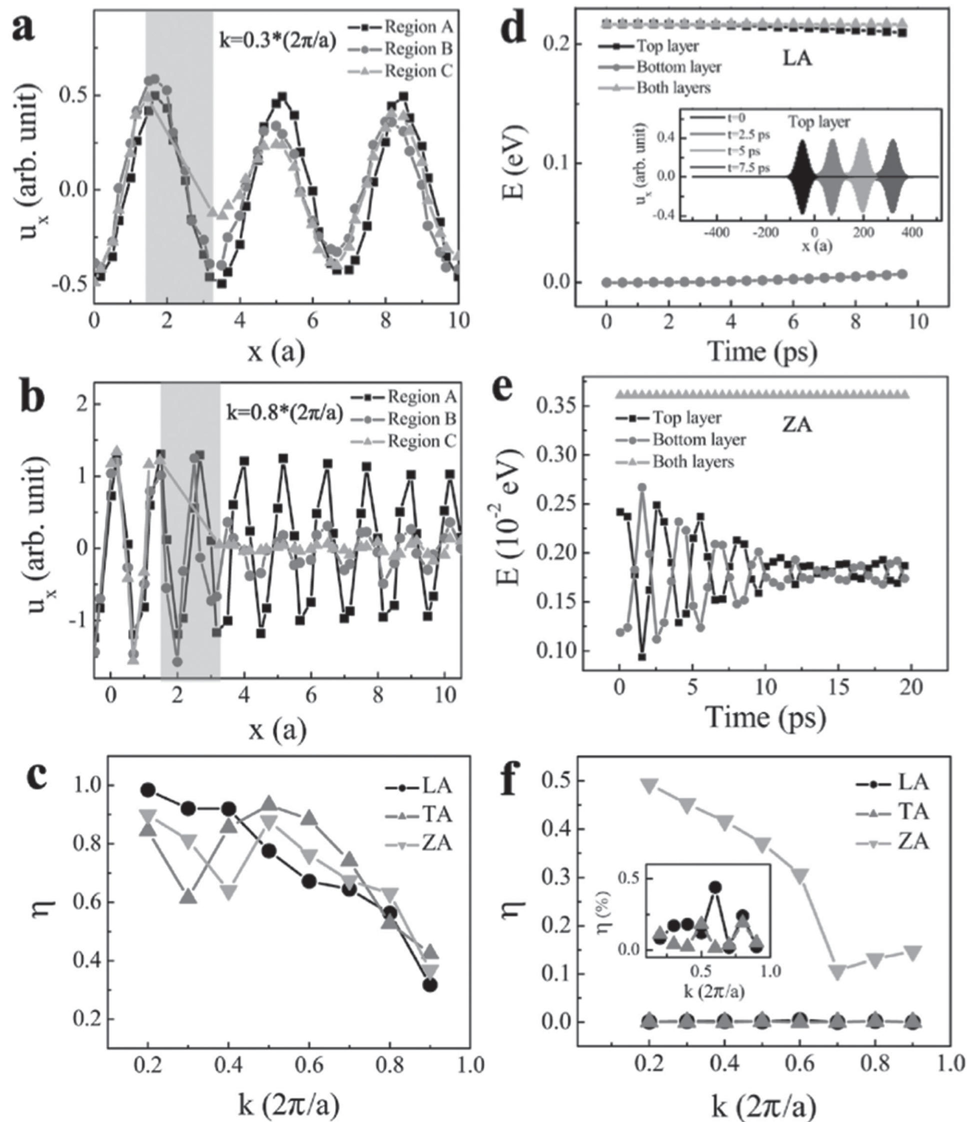

Figure 3. Phonon wave-packet simulation in G-CNT and bilayer graphene. a,b) Atom *x*-displacement in the top graphene layer of the G-CNT for LA phonons with different wavenumbers. Here *a* is the lattice periodicity in the *x*-direction. The regions are defined in Figure 2c. The shadowed region marks the location of CNT with the diameter $D_{CNT} \approx 2a$. c) Phonon energy transmission coefficient η through covalent bonding for different acoustic branches in the [100] direction. d,e) Total energy in bilayer graphene for LA and ZA phonons with $k = 0.2 \times (2\pi/a)$. The inset in panel (d) shows the phonon wave packet in the top layer at different snapshots. f) Phonon energy transmission coefficient η through noncovalent interaction for different acoustic branches in the [100] direction. The inset in panel (f) is a zoom-in for the in-plane acoustic branches. Here results are recorded for the same wave-packet propagation time as in the G-CNT.

(Figure 4b). The computed temperature relaxation times are $\tau = 0.7$ ps and $\tau = 126.6$ ps for the G-CNT and FLG, respectively, exhibiting more than 2 orders of magnitude speed up by the G-CNT. We then immerse the G-CNT in a large water reservoir. Interestingly, the water does not affect the fast heat dissipation path through the solid G-CNT matrix. Furthermore, it removes the heat away from the solid matrix through the solid–liquid interaction and further cools down the hot surface to the ambient temperature. This solid–liquid heat dissipation can be improved by reducing the Kapitza resistance between the solid–liquid interface. We are investigating this aspect in a separate study.[45]

3. Conclusion

In summary, we present a G-CNT hybrid structure that is shown to outperform the heat dissipation properties of both CNTs and FLG by exploiting the covalent bonding of graphene to CNTs. We demonstrate, through MD simulations, that the G-CNT enhances the *c*-axis heat transfer of individual CNTs through their parallel arrangement, while at the same time it provides a large contact area for efficient heat removal. The G-CNT is shown to outperform by 2 to 3 orders of magnitude the heat transfer capabilities of state-of-the-art TIMs. Furthermore, we show that the G-CNT can provide sustained and rapid

© 2015 WILEY-VCH Verlag GmbH & Co. KGaA, Weinheim

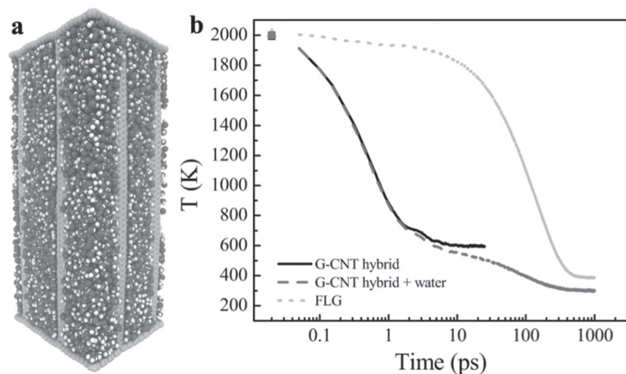

Figure 4. Ultrafast cooling by G-CNT hybrid structure and water. a) The G-CNT immersed in water. b) Averaged temperature of the two hot surfaces cooled down by the G-CNT with/without water surrounded. The cooling performance for FLG is also plotted for comparison. The same cross section of 12×10 nm^2 and thickness of 13 nm in the z-direction are used for both the G-CNT and FLG. The G-CNT has a CNT density $\rho \approx 14\%$, and 46 111 water molecules are used to fill in the empty space between the CNTs. The symbols show the initial temperature of the hot surface.

cooling by being immersed in a liquid. Our results suggest that the proposed G-CNT hybrid can help revolutionize the design of high-performance IC chips.

4. Experimental Section

Thermal Conductivity Calculation: MD simulations in this study were performed using the LAMMPS package,[46] with a time step of 0.5 fs. The sp^2 covalent bonding was modeled by the optimized Tersoff potential[47] for graphene and CNT, which could provide accurate description of the phonon dispersion and thermal conductivity value consistent with the experiment. Lennard–Jones (LJ) potential $V(r) = 4\chi\varepsilon\left[\left(\frac{\sigma}{r}\right)^{12} - \left(\frac{\sigma}{r}\right)^{6}\right]$ with parameters from Girifalco et al.[48] was used to model the noncovalent vdW interaction between CNTs, where χ was a dimensionless scaling factor that controls the interaction strength ($\chi = 1$ by default). The cutoff distance for LJ potential was set as 2.5σ. Equilibrium MD simulations with the NPT ensemble were first performed for structure relaxation and thermal equilibration. NEMD simulations were then carried out to establish the temperature gradient by using the Langevin thermostat. Periodic boundary conditions were applied in the in-plane (xy) directions, and the free boundary condition was used in the z-direction. Thermal conductivity was computed based on Fourier's law $\kappa = -J/\nabla T$, where J was the heat flux computed as the energy induced by the thermostat across unit area per unit time and ∇T was the temperature gradient computed based on the linear regression analysis of the temperature profile. Then NEMD simulation were run long enough (10 ns) to ensure the steady state that temperature gradient and heat flux were independent of time. All results presented in the paper have been averaged over six independent runs with different initial conditions. More details about the simulations and calculations are presented in the Supporting Information.

Phonon Wave-Packet Simulation: Phonon dispersion and eigenvectors in graphene were computed with the optimized Tersoff potential[47] using the GULP package.[49] Following Schelling et al.,[50] the Gaussian wave packets propagating in the [100] direction with different polarizations and wave numbers were applied to the top graphene layer in the G-CNT and to the top graphene layer in bilayer graphene, respectively. In bilayer graphene, the intralayer interaction was covalent and modeled by the short-range optimized Tersoff potential, while the interlayer interaction was noncovalent and modeled by the long-range LJ potential. The width of the wave packet was set as 100 unit cells. The in-plane size of the simulation domain was set as 430×4 nm^2, corresponding to a length of about 1000 unit cells in the propagation direction. A (6,6) CNT with the length of 10 nm was used in the G-CNT structure. Periodic boundary conditions were applied in the in-plane (xy) direction, and the free boundary condition was applied in the z-direction. The phonon transmission coefficient was computed as $\eta = \frac{\Delta E}{\gamma E(0)}$, where ΔE is the energy loss in the top graphene layer, $E(0)$ is the energy of the initial wave packet at time $t = 0$, and γ is a dimensionless factor that accounts for the contact width of the wave packet. For the G-CNT, $\gamma = D_{CNT}/W$, where D_{CNT} is the diameter of CNT and W is the width of the graphene. In bilayer graphene, $\gamma = 1$. More details about the simulation setup and calculations are presented in the Supporting Information.

Liquid Cooling Simulation: The flexible simple point-charge (SPC) water model[51] was used to simulate the water, and the graphene–water interaction was modeled by the LJ potential with parameters from Werder et al.[52] The long-range Coulombic forces were computed by the Particle-Particle-Particle-Mesh (P^{3}M) method[53] with a potential cutoff radius of 9 Å. Periodic boundary conditions were used in all directions. A vacuum region of 4 nm in thickness was added in the z-direction. The whole system was first equilibrated at ambient temperature (300 K) using the NPT ensemble. Then, Langevin thermostats (NVT ensemble) were applied only to the top and bottom graphene layers in both the G-CNT and the FLG to generate two high-temperature (2000 K) hot surfaces. During the heating process, the rest of the atoms in the system were kept fixed. Finally, to simulate the heat dissipation process, thermostats attached to the hot surfaces were removed and all atoms were allowed to move according to the interatomic interactions. To model the infinitely large water reservoir (constant temperature), all the water molecules were thermalized at ambient temperature by using the Langevin thermostat during the heat dissipation process. Following Shenogin et al.,[54] the temperature decay of the hot surface was fitted according to the exponential function $T(t) = T_0 e^{-t/\tau} + y_0$, where τ is the temperature relaxation time that measures the heat dissipation rate.

Supporting Information

Supporting Information is available from the Wiley Online Library or from the author.

Acknowledgements

J.C. acknowledges support as an ETH Zurich Fellow and the EU Marie Curie Actions for People COFUND Program, the startup grant (No. 152225) at Tongji University, and the National Youth 1000 Talents Program in China. Further support was provided by the European Research Council (ERC) Advanced Investigator Award (No. 2–73985–14).

Received: April 20, 2015
Revised: July 9, 2015
Published online:

[1] E. Pop, *Nano Res.* **2010**, *3*, 147.
[2] S. G. Kandlikar, *J. Electron. Packag.* **2014**, *136*, 024001.
[3] R. Prasher, *Proc. IEEE* **2006**, *94*, 1571.
[4] A. A. Balandin, *Nat. Mater.* **2011**, *10*, 569.
[5] S. Ghosh, W. Bao, D. L. Nika, S. Subrina, E. P. Pokatilov, C. N. Lau, A. A. Balandin, *Nat. Mater.* **2010**, *9*, 555.
[6] J. H. Seol, I. Jo, A. L. Moore, L. Lindsay, Z. H. Aitken, M. T. Pettes, X. Li, Z. Yao, R. Huang, D. Broido, N. Mingo, R. S. Ruoff, L. Shi, *Science* **2010**, *328*, 213.
[7] L. Lindsay, D. A. Broido, N. Mingo, *Phys. Rev. B* **2010**, *82*, 161402(R).

© 2015 WILEY-VCH Verlag GmbH & Co. KGaA, Weinheim

DOI: 10.1002/adfm.201501593

[8] S. Chen, Q. Wu, C. Mishra, J. Kang, H. Zhang, K. Cho, W. Cai, A. A. Balandin, R. S. Ruoff, *Nat. Mater.* **2012**, *11*, 203.
[9] M. H. Bae, Z. Li, Z. Aksamija, P. N. Martin, F. Xiong, Z. Y. Ong, I. Knezevic, E. Pop, *Nat. Commun.* **2013**, *4*, 1734.
[10] X. Li, J. Chen, C. Yu, G. Zhang, *Appl. Phys. Lett.* **2013**, *103*, 013111.
[11] M. M. Sadeghi, I. Jo, L. Shi, *Proc. Natl. Acad. Sci. U.S.A.* **2013**, *110*, 16321.
[12] S. Kaur, N. Raravikar, B. A. Helms, R. Prasher, D. F. Ogletree, *Nat. Commun.* **2014**, *5*, 3082.
[13] J. Chen, J. H. Walther, P. Koumoutsakos, *Nano Lett.* **2014**, *14*, 819.
[14] X. Xu, L. F. Pereira, Y. Wang, J. Wu, K. Zhang, X. Zhao, S. Bae, C. Tinh Bui, R. Xie, J. T. L. Thong, B. H. Hong, K. P. Loh, D. Donadio, B. Li, B. Ozyilmaz, *Nat. Commun.* **2014**, *5*, 3689.
[15] B. A. Cola, J. Xu, C. Cheng, X. Xu, T. S. Fisher, H. Hu, *J. Appl. Phys.* **2007**, *101*, 054313.
[16] S. T. Huxtable, D. G. Cahill, S. Shenogin, L. Xue, R. Ozisik, P. Barone, M. Usrey, M. S. Strano, G. Siddons, M. Shim, P. Keblinski, *Nat. Mater.* **2003**, *2*, 731.
[17] Z. Han, A. Fina, *Prog. Polym. Sci.* **2011**, *36*, 914.
[18] R. Gulotty, M. Castellino, P. Jagdale, A. Tagliaferro, A. A. Balandin, *ACS Nano* **2013**, *7*, 5114.
[19] A. A. Balandin, S. Ghosh, W. Bao, I. Calizo, D. Teweldebrhan, F. Miao, C. N. Lau, *Nano Lett.* **2008**, *8*, 902.
[20] M. Harb, C. von Korff Schmising, H. Enquist, A. Jurgilaitis, I. Maximov, P. V. Shvets, A. N. Obraztsov, D. Khakhulin, M. Wulff, J. Larsson, *Appl. Phys. Lett.* **2012**, *101*, 233108.
[21] G. K. Dimitrakakis, E. Tylianakis, G. E. Froudakis, *Nano Lett.* **2008**, *8*, 3166.
[22] Y. Zhu, L. Li, C. Zhang, G. Casillas, Z. Sun, Z. Yan, G. Ruan, Z. Peng, A. R. Raji, C. Kittrell, R. H. Hauge, J. M. Tour, *Nat. Commun.* **2012**, *3*, 1225.
[23] R. Lv, E. Cruz-Silva, M. Terrones, *ACS Nano* **2014**, *5*, 4061.
[24] V. Varshney, S. S. Patnaik, A. K. Roy, G. Froudakis, B. L. Farmer, *ACS Nano* **2010**, *4*, 1153.
[25] J. Lee, V. Varshney, J. S. Brown, A. K. Roy, B. L. Farmer, *Appl. Phys. Lett.* **2012**, *100*, 183111.
[26] J. Park, V. Prakash, *J. Appl. Phys.* **2014**, *116*, 014303.
[27] M. Fujii, X. Zhang, H. Xie, H. Ago, K. Takahashi, T. Ikuta, H. Abe, T. Shimizu, *Phys. Rev. Lett.* **2005**, *95*, 065502.
[28] J. Yang, S. Waltermire, Y. Chen, A. A. Zinn, T. T. Xu, D. Li, *Appl. Phys. Lett.* **2010**, *96*, 023109.
[29] G. Zhang, B. Li, *J. Chem. Phys.* **2005**, *123*, 114714.
[30] J. Shiomi, S. Maruyama, *Jpn. J. Appl. Phys.* **2008**, *47*, 2005.
[31] C. Chang, D. Okawa, H. Garcia, A. Majumdar, A. Zettl, *Phys. Rev. Lett.* **2008**, *101*, 075903.
[32] N. Yang, G. Zhang, B. Li, *Nano Today* **2010**, *5*, 85.
[33] B. A. Cola, *Electronics Cooling* **2010**, *16*, 10.
[34] B. Choi, E. Lee, D. Whang, B. Kim, *US Patent US 2011/0121264 A1*, **2011**.
[35] D. I. Barker, W. R. Owens, J. W. Beck, *USA Patent US 2012/0152725 A1*, **2012**.
[36] J. M. Tour, Y. Zhu, L. Li, Z. Yan, J. Lin, *World Patent WO 2013/119295 A1*, **2013**.
[37] K. M. Shahil, A. A. Balandin, *Nano Lett.* **2012**, *12*, 861.
[38] V. Goyal, A. A. Balandin, *Appl. Phys. Lett.* **2012**, *100*, 073113.
[39] Z. Yan, D. L. Nika, A. A. Balandin, *IET Circuits, Devices & Systems* **2015**, *9*, 4.
[40] B. Koo, P. Goli, A. V. Sumant, P. C. d. S. Claro, T. Rajh, C. S. Johnson, A. A. Balandin, E. V. Shevchenko, *ACS Nano* **2014**, *8*, 7202.
[41] H. Bao, C. Shao, S. Luo, M. Hu, *J. Appl. Phys.* **2014**, *115*, 053524.
[42] Z.-Y. Ong, E. Pop, *Phys. Rev. B* **2011**, *84*, 075471.
[43] J. Chen, G. Zhang, B. Li, *Nanoscale* **2013**, *5*, 532.
[44] B. Qiu, X. Ruan, *Appl. Phys. Lett.* **2012**, *100*, 193101.
[45] D. Alexeev, J. Chen, J. H. Walther, K. P. Giapis, P. Angelikopoulos, P. Koumoutsakos, *Nano Lett.* **2015**, *15*, 5744.
[46] S. Plimpton, *J. Comput. Phys.* **1995**, *117*, 1.
[47] L. Lindsay, D. A. Broido, *Phys. Rev. B* **2010**, *81*, 205441.
[48] L. A. Girifalco, M. Hodak, R. S. Lee, *Phys. Rev. B* **2000**, *62*, 13104.
[49] J. D. Gale, *J. Chem. Soc., Faraday Trans.* **1997**, *93*, 629.
[50] P. K. Schelling, S. R. Phillpot, P. Keblinski, *Appl. Phys. Lett.* **2002**, *80*, 2484.
[51] Y. Wu, H. L. Tepper, G. A. Voth, *J. Chem. Phys.* **2006**, *124*, 024503.
[52] T. Werder, J. H. Walther, R. L. Jaffe, T. Halicioglu, P. Koumoutsakos, *J. Phys. Chem. B* **2003**, *107*, 1345.
[53] R. W. Hockney, J. W. Eastwood, *Computer Simulation Using Particles*, CRC Press, Boca Raton, FL, USA **1988**.
[54] S. Shenogin, L. Xue, R. Ozisik, P. Keblinski, D. G. Cahill, *J. Appl. Phys.* **2004**, *95*, 8136.

© 2015 WILEY-VCH Verlag GmbH & Co. KGaA, Weinheim